Swanson, H. L.; Pokhrel, S.; Davidowski, S. K.; Mädler, L.; Brinker, C. J.; Holland, G. P.

The Impact of Metal Doping on Fumed Silica Structure and Amino Acid Thermal Condensation Catalytic Properties

Recommended Citation (primary publication/Version of Record) incl. DOI:

Swanson, H.L., Pokhrel, S., Davidowski, S.K. et al. The impact of metal doping on fumed silica structure and amino acid thermal condensation catalytic properties. J Mater Sci 56, 16916–16927 (2021). https://doi.org/10.1007/s10853-021-06412-0

The Impact of Metal Doping on Fumed Silica Structure and Amino Acid Thermal Condensation Catalytic Properties

Haley L. Swanson,[a] Suman Pokhrel,[b,c] Stephen K. Davidowski,[d] C. Jeffrey Brinker,[e,f] and Gregory P. Holland[*a]

[a]Department of Chemistry and Biochemistry, San Diego State University, 5500 Campanile Drive, San Diego CA 92182-1030, USA
[b]Department of Biological Sciences, University of New Orleans, New Orleans LA 70148, USA
[c]Department of Chemistry, University of New Orleans, New Orleans LA 70148, USA
[d]Department of Chemistry and Biochemistry, Magnetic Resonance Research Center, Arizona State University, Tempe AZ 85287-1604, USA
[e]Center for Micro-Engineered Materials, Advanced Materials Laboratory, University of New Mexico, 1001 University Blvd SE, Suite 103, Albuquerque NM 87106, USA
[f]Department of Chemical and Biological Engineering, University of New Mexico, 210 University Blvd NE, Albuquerque NM 87131-0001, USA

Abstract

Fumed silica nanoparticles (FSN) are one of the most commonly synthesized forms of silica but prolonged exposure leads to cell toxicity and apoptosis due to reactive oxygen species (ROS) generation inherent to these particles. Increasing attention is being made on making the material safer both for workers involved in large-scale industrial production, and consumers coming into contact with fumed silica additives. In the present work, we explore the structural differences and efficacy of Al- and Ti- metal doped FSN which has previously been shown to reduce toxicity effects of the nanoparticles. We use a combination of ^{29}Si and ^{27}Al solid-state magic angle spinning (MAS) NMR, Raman spectroscopy, and thermogravimetric analysis (TGA) to analyze changes in the bulk of the nanomaterials and quantify the adsorption capacity and reactivity of the surface with respect to amino acid thermal condensation. Alanine was selected as the ligand of choice for its simplicity and ubiquity in biochemical reactions. Our results indicate that metal doping has a modest impact on the fumed silica structure, ligand adsorption capacity, and thermal condensation however, metal dopings of 1-7% perform comparably to commercial fumed silica.

Key words

1. Introduction

Fumed silica nanoparticles (FSN) are generally recognized as safe (GRAS) by the Food and Drug Administration (FDA) and is a common anti-caking additive in foods, beverages, and cosmetics used for decades [1]. However, recent data shows that repeated exposure leads to accumulation in cells, causing inflammation and apoptosis [2-4]. It has been hypothesized that this is due to strained ring defects inherent to FSN and that these strained rings can easily cleave to form radicals that are highly reactive and toxic to cells [2,5]. A few groups have begun addressing this issue, and one promising alternative is the inclusion of metal doping which has been shown to decrease toxic radical generation [3,4]. In the present work, we analyze aluminum and titanium-doped FSN using solid-state nuclear magnetic resonance (SSNMR), Raman spectroscopy, and thermogravimetric analysis (TGA) to determine the impact of metal doping on FSN bulk structure, adsorption capacity and reactivity. Brunauer-Emmett-Teller (BET) and TGA are used to quantify the loading capacity.

One of the reasons why FSN is such an efficient thickening agent is because of its extremely high surface area with primary particle sizes in the range of 7 – 14 nm. The high surface area combined with reactive oxygen species (ROS) generation makes it a very effective metal oxide catalyst in the promotion of thermal condensation reactions which have implications in origin of life research [6-12]. Much of the Earth's crust is comprised of silicates, silica-containing clays and silica substrates have been shown to sequester and stabilize amino acids in dilute solutions and promote oligomerization [8,13-15]. The oligomerization proceeds through condensation of neighboring amino acids and is readily monitored by first derivative thermogravimetric analysis (DTG) [13,16-19]. This presents a simple and effective method to monitor changes in surface reactivity as doping level increases.

The aim of this investigation is to determine if Al- and Ti- metal doping, which has been shown to effectively decrease cell toxicity in recent studies, can still maintain similar function when interacting with ligands at the surface and how the surface sites change [3,4]. We expect to see decreased similarities to undoped FSN (0%FSN) as doping levels increase from 1 – 10%, with homogenous incorporation of the metal into the framework. Less perturbation is expected in

2

Ti- doped samples based on its coordination state being most similar to Si^{4+}. If changes are minimal, this would provide an effective and safer alternative for FSN exposure.

2. Experimental Section

Materials

Natural abundance L-alanine was purchased from Sigma-Aldrich and used as recieved.

2.1 Synthesis

2.1.1 Preparation of Metal-Doped FSN

Flame spray pyrolysis was used to synthesize metal-doped silica nanoparticles. Details of the procedure are described elsewhere [3,4].

2.1.2 Adsorption of Alanine on FSN

FSN was heated at 500 °C in an oven overnight to remove impurities from the surface and activate the FSN. Aqueous solutions of alanine were produced [0.10M] using deionized water and separated into 5.00 mL aliquots. 75 mg of FSN was added and each solution was stirred overnight at ambient conditions followed by centrifugation at 6000 rpm for 1 hr to pellet the adsorption complex. Samples were dried under vacuum overnight at room temperature and analyzed as described below.

2.2 Characterization

2.2.1 Solid-state Nuclear Magnetic Resonance Spectroscopy

NMR experiments were conducted with a 600 MHz Bruker Avance IIIHD spectrometer equipped with a 4 mm double resonance (^{1}H/X) MAS probe. ^{27}Al direct polarization (DP)-MAS experiments were collected with 15 kHz MAS using a 0.66 μs (π/12) excitation pulse, 1600 ppm spectral width (sw), 4k points, 0.25 sec recycle delay (d1), and 16k – 256k scans, with no decoupling. ^{27}Al CP-MAS experiments were collected at 15 kHz MAS with an 800 ppm sw, 512 points, 1 sec d1, 16k scans, with no decoupling. An initial ^{1}H π/2 pulse of 4.5 μs was used

followed by a 30% ramped 500 μs contact pulse matched to the -1 Hartman Hahn spinning side band condition for ^{27}Al of 35 kHz B_1 field strength (RF). ^{27}Al spectra were processed with 2k points, 100 Hz line broadening and externally referenced to a 1M solution of $Al(NO_3)_3$ (0 ppm). Aluminum oxide was used to set up CP-MAS experiments.

^{29}Si DP-MAS experiments were collected at 5 kHz MAS using a 4 μs (π/2) excitation pulse, 382 ppm sw, 512 points, 300 sec d1, and 280 scans. High-powered spinal-64 ^1H decoupling was applied at 44 – 46 kHz RF during acquisition and spectra were processed with 4k points and 50 Hz line broadening. ^1H → ^{29}Si cross-polarization (CP) experiments included an initial ^1H π/2 pulse of 2.7-2.75 μs followed by a ramped (50%) 5 ms contact pulse matched to the -1 Hartman Hahn spinning sideband condition for ^{29}Si at 55 kHz RF. High-powered spinal-64 ^1H decoupling at 44 – 46 kHz RF was applied during acquisition. ^{29}Si CP-MAS experiments were collected with a 382 ppm sw, 512 points, 5 sec d1, and 8k scans. 20 Hz line broadening and zero-filling to 2k points were used in processing. All ^{29}Si spectra were externally referenced to TTSS (-9.7 ppm).

2.2.2 Raman Spectroscopy

The Raman spectroscopic data was collected using a custom-built Raman spectrometer in 180° geometry. The sample was excited using a 150 mW Coherent Sapphire SF laser with a 532 nm laser wavelength. The laser power was controlled using a neutral density filter wheel and an initial laser power of 28 mW. The laser was focused onto the sample using a 50X super long working distance plan APO Mitutoyo objective with a numerical aperture of 0.42. The signal was discriminated from the laser excitation using a an Ondax® SureBlock™ ultranarrow-band notch filter combined with two Optigrate notch filters. The data was collected using an Acton 300i spectrograph and a back thinned Princeton Instruments liquid nitrogen cooled CCD detector.

2.2.3 Thermogravimetric Analysis

A TA2910 (TA Instruments Inc.) TGA was used to quantify adsorption and assess surface reactivity of the metal doped FSN. A sample mass of 12 – 15 mg was used in each experiment and the sample was equilibrated under N_2 flow for a minimum of 30 min prior to analysis or until a stable baseline was reached. The instrument flow rate was maintained at 60 mL/min and 40 mL

min^{-1} for furnace and balance, respectively. The TGA method included temperature equilibration at 25 °C followed by a 5 °C min^{-1} heating rate applied from 25 – 600 °C.

3. Results

3.1 Solid-State NMR

^{29}Si CP-MAS

^{1}H → ^{29}Si CP-MAS experiments were used to selectively characterize the surface of FSN since the bulk material is composed of siloxane bonds (excluding minor defects and trapped interparticle water) and the only proton spin bath comes from surface silanols making the method surface specific [20]. In a typical ^{29}Si CP-MAS spectrum, three peaks are present centered at -90 ppm (Q_2), -100 ppm (Q_3), and -110 ppm (Q_4) where the number represents the number of bridging siloxane bonds in a tetrahedrally coordinated silicon atom. In zeolites and other silicates, R coordinated sites are expected at -50 ppm (T_1), -60 ppm (T_2), and -70 ppm (T_3) [21,22]. T_n sites represent direct Si-R coordination. No T_n sites were observed in any of the doped spectra, indicating that the metal atoms are incorporated into the siloxane network replacing tetrahedrally coordinated silicon and attaching to bridging oxygens.

^{29}Si CP-MAS spectra (Figure 1, Table 1) were fit with the software package MestreNova. No major differences in peak shapes were observed. The full width at half maximum (FWHM) increased with increased doping level for all Q_n sites in Al containing samples, with 10% exhibiting the largest FWHM. Compared to 0%FSN, the FWHM increased by ~65 Hz (Q_2), ~105 Hz (Q_3), ~260 Hz (Q_4). All sites are broadened indicating that Al is incorporated near the surface and in Q_4 sites near the surface. A smaller overall change in FWHM is observed across Ti-dopants and 10%Ti only increases by ~7 Hz (Q_2), ~12 Hz (Q_3), and ~145 Hz (Q_4) compared to 0%FSN. The FWHM actually decreased in Q_2 by ~10 Hz from 1-7%Ti, in Q_3 by ~10 Hz from 1-3%Ti, and in Q_4 by ~15 Hz from 5-7%Ti. The FWHM was slightly higher in Al-dopings vs Ti-dopings presumably due to the nominal charge difference where Al is +3 and Ti +4. Overall, the increase in linewidth with metal doping content indicates an increase silica disorder with Al containing samples being the most disordered.

The relative abundances of Q_n sites were also analyzed and only minimal differences in Q_n ratios were observed. For Al-dopants, Q_2 populations remain the same across samples and Q_3 is converted to Q_4 as doping level increases assuming similar CP efficiency across samples. This is

another indication that some of the aluminum sites may be congregating near the surface. In Ti-dopants, Q_3 gets converted to Q_2 and Q_4 but the changes are still minimal in comparison to Al. Lastly, chemical shift was analyzed and changes are small (~0.5 to 1 ppm) but trend downfield with increasing dopant indicating a small decrease in T-O-T bond angle [23,24].

Overall, the absence of any T_n sites among dopants confirms that the metal is incorporated into the framework through bridging oxygens. The FWHM all Q_n sites increases at the 10% level which suggest that at least some of the dopants are near the surface. Al dopants create a larger change in CP-MAS spectra than Ti dopants suggesting that Al makes the framework more amorphous.

Table 1. SSNMR data from [29]Si CP-MAS of doped spectra.

	Q_2			Q_3			Q_4		
	Abundance	FWHM (Hz)	δ (ppm)	Abundance	FHWM (Hz)	δ (ppm)	Abundance	FWHM (Hz)	δ (ppm)
0% FSN	0.14	645	-91.0	0.69	881	-100.4	0.17	985	-110.4
1% Al	0.14	656	-91.0	0.66	882	-100.2	0.20	1050	-109.8
3% Al	0.15	656	-90.7	0.63	890	-99.8	0.21	1115	-109.3
5% Al	0.15	661	-90.6	0.60	939	-99.5	0.24	1164	-108.9
7% Al	0.15	675	-90.8	0.62	944	-99.6	0.23	1089	-108.8
10% Al	0.15	711	-90.7	0.59	986	-99.7	0.26	1246	-109.1
1% Ti	0.13	620	-91.5	0.66	875	-100.8	0.21	1014	-110.5
3% Ti	0.13	614	-91.5	0.64	865	-100.7	0.23	1108	-110.2
5% Ti	0.14	613	-91.0	0.62	874	-100.2	0.24	1112	-109.7
7% Ti	0.14	609	-90.7	0.62	886	-99.9	0.24	1096	-109.5
10% Ti	0.15	652	-91.0	0.62	893	-100.2	0.23	1129	-109.9

a)

0%FSN
1% Al
3% Al
5% Al
7% Al
10% Al

^{29}Si Chemical Shift (ppm)

b)

0%FSN
1% Ti
3% Ti
5% Ti
7% Ti
10% Ti

^{29}Si Chemical Shift (ppm)
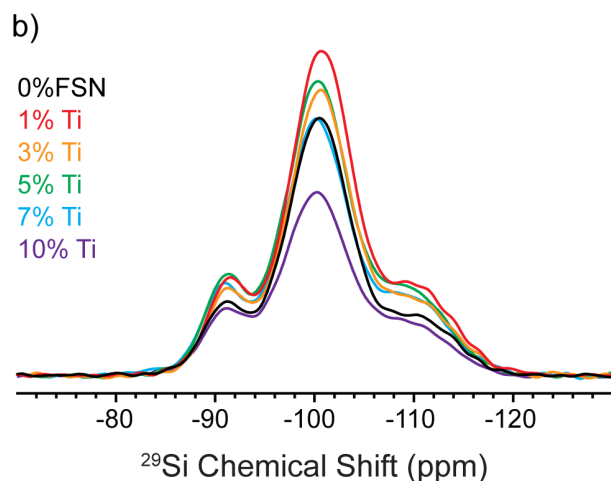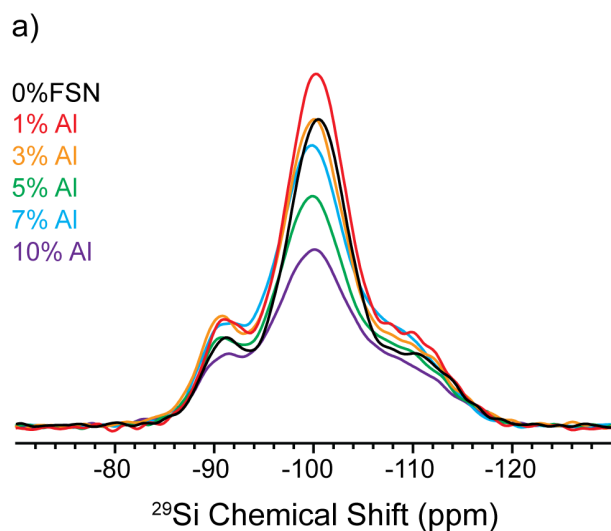
Figure 1. ^{29}Si CP-MAS NMR of Al- and Ti-doped samples with 0%FSN. Spectra are scaled proportionally to sample mass.

^{29}Si DP-MAS NMR

^{29}Si DP-MAS NMR (Figure 2) was utilized to examine bulk structural changes for FSN samples as a function of metal doping. Due to the low signal intensity of protonated Q_2 and Q_3 sites in ^{29}Si DP-MAS experiments, the discussion will focus on Q_4 resonances that dominate the spectra and represent the bulk siloxane bonds. A long recycle delay (300 sec) was used and spectra were scaled by mass for quantitative analysis. All samples had a broad Q_4 resonance due to the intrinsic amorphous nature of FSN. Since DP-MAS is a direct polarization technique and proton decoupling was applied during acquisition, broadening can be attributed to the degree of

disorder within the bulk framework similar to the above discussions for CP-MAS results, specifically a larger distribution of Si-O-T (T=Al, Si, or Ti) bond angles and Si-O bond strengths, as well as Al and Ti disorder from the presence of multiple coordination sites (see [27]Al discussion below). While Al and Ti are the next nearest neighbors (NNN) (i.e. not directly bound to silicon), they do have a deshielding effect on the observed ^{29}Si NMR isotropic chemical shift [23,25-27].

a)

0%FSN
1% Al
3% Al
5% Al
7% Al
10% Al

-80   -90   -100   -110   -120

[29]Si Chemical Shift (ppm)

b)

0%FSN
1% Ti
3% Ti
5% Ti
7% Ti
10% Ti

-80   -90   -100   -110   -120

[29]Si Chemical Shift (ppm)
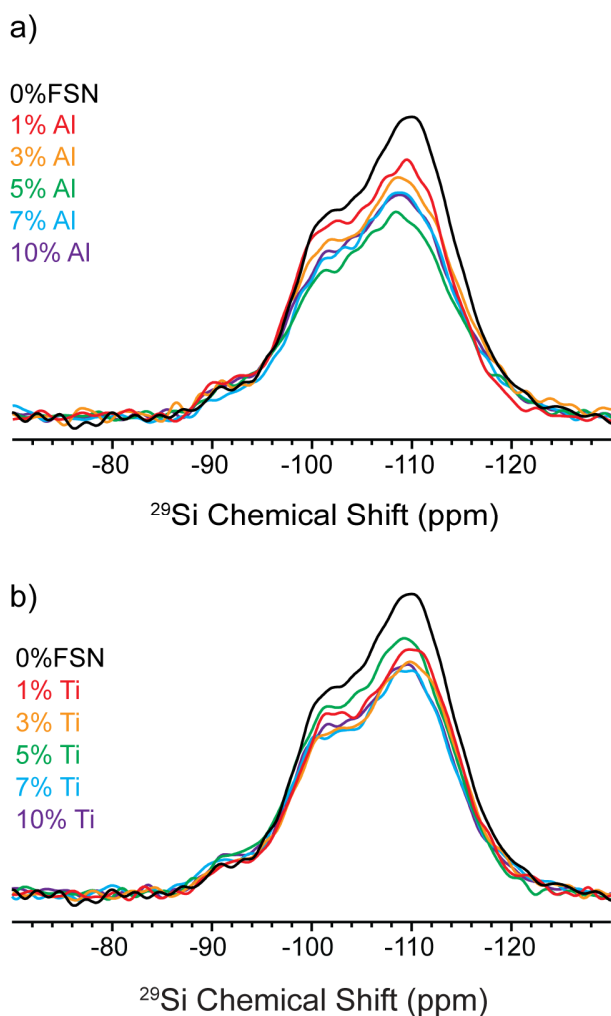
Figure 2. ^{29}Si DP-MAS NMR of Al- and Ti-doped samples with 0%FSN.

In Al-doped samples, Q_4 intensity decreases as doping level increases from 1% to 5% indicating homogenous incorporation in the framework with increasing formation of Si-O-Al bonds. While aluminum is commonly found in multiple coordination environments, titanium is

8

typically octahedrally coordinated as the rutile polymorph [28]. However, previous studies have shown that at low metal doping levels in titanium-containing silicate glasses (0.05 < TiO_2 < 9 % (w/w)) the titanium cations are primarily tetrahedral with increasing levels of octahedral coordination as doping level increases [29-31]. [29]Si Q_4 intensities of Ti-doped samples are scattered and no trends can be established (Figure 2). It is interesting to note that the 5% doping in both materials are outliers. 5%Ti has the largest Q_4 population after 0%FSN, followed by 1%Ti, then 3%/7%/10%Ti with the lowest. The absence of any trend or large change in Q_4 peak area and chemical shift suggests that Ti- is either phase separated from the Si-O-T network or that is is not incorporaed in the framework at all. This will be discussed further in the Raman section.

In addition to changes in Q_4 intensity, Q_4 resonances shift downfield as doping level increases. Many studies have been done that relate ^{29}Si DP-MAS NMR isotropic chemical shifts to Si-O-Si bond angle [23,24,26,32-34]. In this work, we used the equation published by Smith and Blackwell [34] derived from silica polymorphs and later applied to amorphous FSN by Legrand et al [24] to estimate the average Si-O-T bond angle of each dopant that is listed in Table 2 for the samples studied here. As the siloxane bond angles decrease, silicon atoms become deshielded and Q_4 shifts downfield. However, it is important to note that aluminum and titanium also have deshielding effects as NNN and likely contribute to the Q_4 shift downfield [25,27]. Therefore, the chemical shift cannot be attributed to differences in bond angle alone. The total downfield shift from 0%FSN to 10%Al or 10%Ti is small (~ 1 ppm) although the trend would likely continue if doping levels were increased further. This is consistent with the results published by Ramdas et al, where ~ 5 ppm shift is observed in 25% Al content of zeolites and with Balmer et al, where a 5 – 10 ppm shift is observed at 25% Ti doped silica glass [25,27].

Table 2. ^{29}Si Q$_4$ isotropic chemical shift from DP-MAS and predicted Si-O-T bond angle calculated from Smith & Blackwell.

	Al-doped (δ ppm)	α	Ti-doped (δ ppm)	α
0%FSN	-110.0	146.9	-110.0	146.9
1%	-109.6	146.4	-109.9	146.7
3%	-108.5	145.0	-109.7	146.5
5%	-108.3	144.8	-108.9	145.5
7%	-108.7	145.2	-109.4	146.1
10%	-108.8	145.4	-109.1	145.7

^{27}Al DP-MAS NMR

^{27}Al MAS NMR is a useful technique for determining aluminum coordination. Due to limited sample quantity, only 1%, 5% and 10% Al were analyzed, as well as 10%Al following thermal treatment (overnight at 500 °C), rehydration, and adsorption of Ala (Figure 3). In all samples, at least three Al resonances are observed ~ 52, 12 and 0 ppm indicating a presence of tetrahedral (52 ppm) and a minimum of two octahedral coordination sites (12, 0 ppm). A large broad resonance is observed in all samples ~ 33 ppm. It is unclear whether this is due to the presence of a penta-coordinated species or second-order quadrupolar interactions of additional tetrahedral site [35-37]. The center of this resonance does not shift with doping level and remains present even following calcination and rehydration of 10%Al. We hypothesize that it is likely due to quadropolar interactions because penta-coordinated sites are less common and are often unobservable due to the asymmetric nature of the site [38-40]. Additionally, in the literature Al[O$_5$] sites were only observed in very high aluminum percentages (30% and 70%Al) as was shown previously for Al-doped FSN [39] and in zeolites (ZSM-5 and HZSM-5) following thermal treatment over 900 °C and rehydration [38,40].
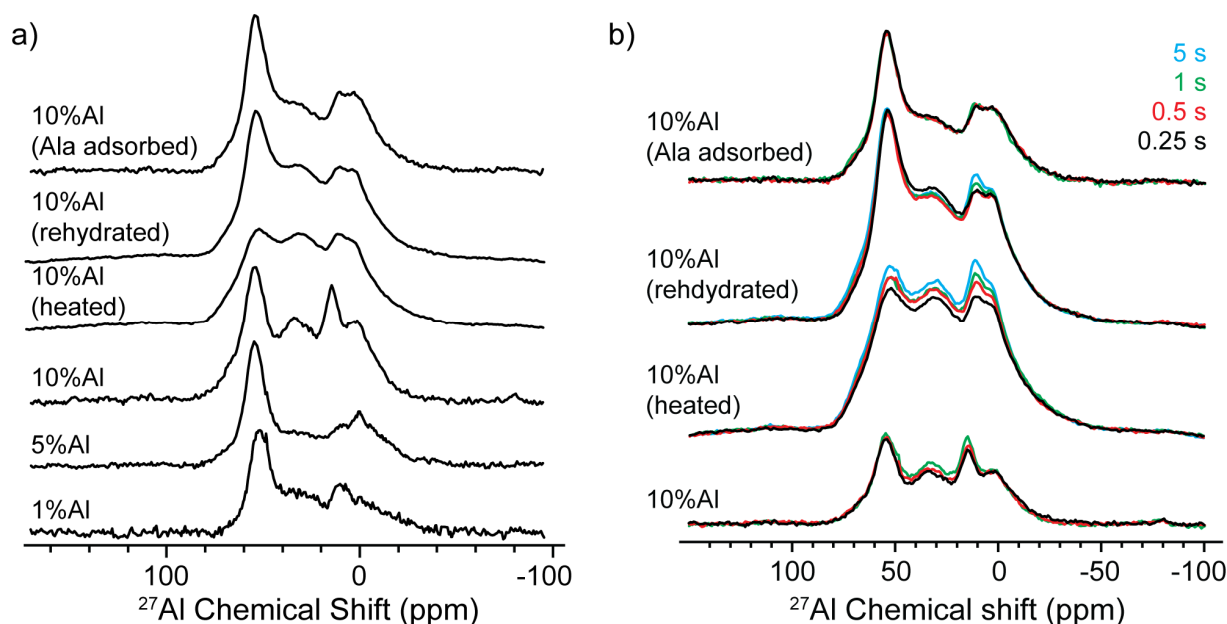
Figure 3. ^{27}Al DP-MAS NMR of Al-doped samples. Spectra were collected at 15 kHz MAS. A recycle delay of (a) 0.25 sec and (b) variable delay between 0.25 and 5 sec were used.

[27]Al is a quadrupolar nuclei, meaning local symmetry has a large effect on signal intensity and powder pattern lineshapes, so peak area is not indicative of relative populations [41,35,36]. Typically, octahedrally coordinated sites have high symmetry and exhibit only first order quadrupolar contributions to the resonances with little to no second order contribution and is expected to have a stronger signal intensity [41,35,36]. However, the metal doping levels analyzed here are all dominated by tetrahedrally coordinated $Al[O_4]$ (~ 52 ppm). This is expected since aluminum atoms are replacing silicon in a tetrahedrally coordinated environment. 1%Al and 5%Al appear mostly tetrahedral, and 10%Al has strong contributions from both tetrahedral and octahedral regions.

In our $10\%Al\text{-}SiO_2$ sample, there is not much change after heating. The tetrahedral and octahedral horns broaden due to disorder and restricted dynamics. Heating impacts T_1 relaxation of all sites which we observe by the peak intensities increasing with increasing recycle delay (see Figure 3). After rehydration, only the downfield octahedral horn shows changes with increasing recycle delay, which suggests that this site is in the framework and unaffected by local dynamics or rearrangement at the surface after rehydration. [27]Al CP-MAS was also collected on 10%

heated and rehydrated (discussed in the next section), and the upfield octahedral site has the largest CP signal, suggesting this site is close to or at the surface.

In addition to ^{29}Si, ^{27}Al resonances are also deshielded with increasing %Al. While we cannot accurately report chemical shifts from a basic Lorentizan Gaussian linefit, it is obvious that the horns in the Al[O$_4$] and Al[O$_6$] regions shift downfield as doping level increases. Al[O$_4$] shifts <1 ppm from 5% to 10% and <1 ppm after calcination and rehydration supporting that aluminum was homogenously incorporated in the framework. The Al[O$_6$] site, however, shifts 5 ppm downfield from 1% to 10% which could mean that the octahedral sites are potentially the result of phase-separation. If ^{27}Al nuclei are deshielded with increasing aluminum content, this means either an increase in ^{27}Al NNN (more Al-O-Al bonds) or Al nuclei are sensitive to the long-range electron withdrawing effects (less likely). The idea of phase-separation is in agreement with ^{29}Si DP-MAS which shows a slight increase in ^{29}Si Q$_4$ content at 10%Al.
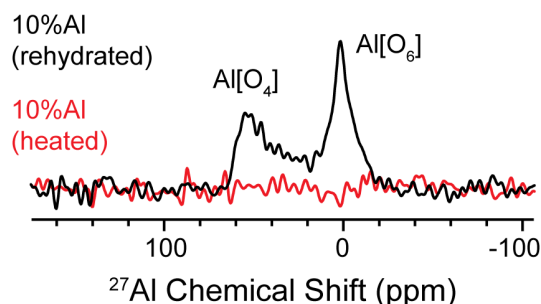
Figure 4. ^{27}Al CP-MAS NMR of 10%Al- doped samples after heating and rehydration.

^{27}Al CP-MAS

^{27}Al CP-MAS was collected on 10%Al heated and rehydrated (Figure 4). No signal was observed in the heated sample when a short contact pulse was used (500 μs). Al[O$_4$] and some Al[O$_6$] sites repopulated after rehydration. We interpret this to mean the upfield Al[O$_6$] peak is directly coordinated with water or cleave to form surface hydroxyls and some Al[O$_4$] sites are near the surface close to the proton spin bath but may not be directly bound. Aluminum hydroxides are present in penta and octahedrally coordinated materials [42,39,43].

3.2 Raman Spectroscopy

The Raman spectra of 0%FSN displays characteristic silica stretching modes (oxygen bending motion in the random network denoted as "R" ~ 440 cm^{-1}, stretching vibrations of Si-O-Si ~ 800 cm^{-1}, and Si-(OH) stretching ~ 950 cm^{-1}) and strained defects (oxygen breathing vibrations of strained 4- and 3- membered rings denoted as "D1" ~ 495 cm^{-1} and "D2" ~ 605 cm^{-1}, respectively) [44,45]. Al-doped samples produced too much fluorescence for analysis (Figure S1) so only Ti-doped samples will be discussed here. Five of the 6 Raman active anatase stretching modes were observed in all Ti-doped samples with no evidence of rutile coordination (Figure 5). Previous studies on Ti-doped FSN found that octahedral coordination is preferred in Ti >9%, and that either rutile or anatase coordination is possible and is determined by the mode of glass preparation [29,30]. Silicon is a known inhibitor of rutile transformation so it is not surprising that anatase is observed even though rutile is the thermodynamically and kinetically stable polymorph [28]. The anatase stretching modes dominate all Ti-dopants and convolute the silica defects making them unobservable. 5%Ti has the weakest anatase peaks which is in agreement with ^{29}Si DP-MAS that show 5% has the largest ^{29}Si Q$_4$ intensity. Surprisingly, the silica stretching modes are most pronounced in 10%Ti-SiO$_2$ where anatase peaks are also the strongest. This supports that phase separation is a strong possibility for the Ti-doped samples and is also consistent with little change observed in the ^{29}Si MAS NMR results discussed above. Anatase is crystalline and the peaks in 10%Ti are significantly more intense than any of the other dopings. This would also explain the increase in silica stretching modes as well for this sample.

In Balmer et al's analysis of the titanosilicate pollucite (CsTiSi$_2$O$_{6.5}$) Ti- and Si- stretching and bending modes were significantly broadened and convoluted [27]. Huang et al analyzed amorphous TiO$_2$ xerogel as well as crystalline anatase and rutile polymorphs [46]. In the amorphous form the peaks are so broad they are unresolvable. The anatase peaks in our doped samples looks like that of pure crystalline anatase leading to the conclusion that anatase is the primary containing component of the sample and incorporation into the FSN framework through Si-O-T bonding is low.
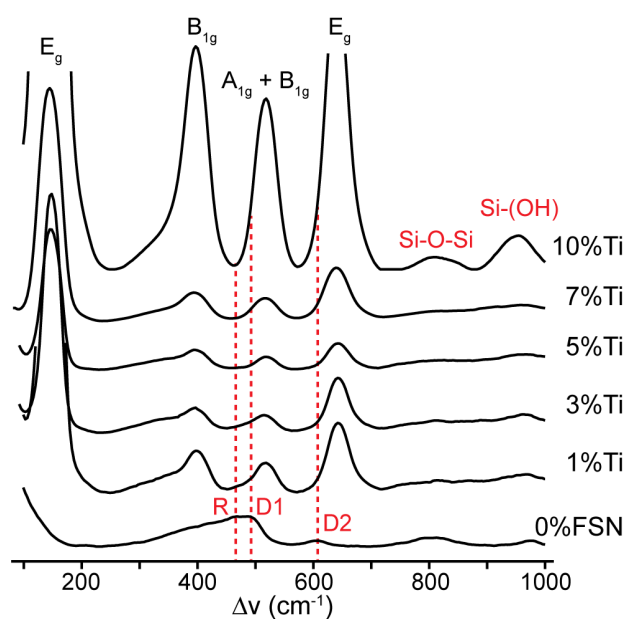
Figure 5. Raman spectra of 0%FSN and Ti-doped FSN.

3.3 Thermal Analysis

TGA

TGA monitors sample weight loss as a function of temperature and can be used to determine the amount of adsorbed water and organic species. TGA can also be used to observe thermal condensation reactions for adsorbed amino acids by detecting the water loss during the formation of peptide bonds [13,14,47-50]. Because of the limited amount of material only two TGA runs could be conducted per metal doped FSN sample. Some variation exists within each sample depending on environmental humidity, starting temperature of furnace, and N_2 tank pressure. The most notable difference between samples is observed when one is the first run of the day. The starting temperature is a few degrees lower than subsequent runs which dries sample slightly and removes more of the surface water. Samples that were collected as the first run of the day have an inflated water loss, so data from the second run was used in calculations. The average of both runs was also calculated and did not greatly impact the results.

The hydroxyl content (OH nm^{-2}), primary particle size (nm), and surface area (m^2 g^{-1}) were quantified by BET and are reported in Table 3. Together, these values determine the number of available ligand binding sites which is one of the primary traits that determine the amount of Ala that will bind. The weight loss reported in Table 3 is the loss of Ala, measured

from 100 – 600 °C. All doped NPs were within ± 1% of 0%FSN indicating that doping level has little effect on the amount of adsorbed alanine. The average weight loss, quantified by TGA (Figure S2) was 6.47% for 0%FSN, 7.07 ± 0.37% (Al-doped NPs), and 6.80 ± 0.56% (Ti-doped NPs). The average of both Al- and Ti- dopants were higher than 0%FSN and both had small standard deviations. This again shows that doping slightly increases the amount adsorbed and little variation exists between 1% and 10% dopants added.

One of the properties that make FSN unique is its efficacy in catalyzing the thermal condensation and oligomerization of adsorbed amino acids [17-19,50-52]. The first derivative thermogram (DTG) was analyzed where peptide bond formation is easily visualized by a peak ~ 165 °C caused by water loss from the thermal condensation (TC) of neighboring molecules [13,14,16,18,19,50,53,54]. Guo et al found that FSN converts alanine into the dipeptide alanine anhydride with nearly 100% efficiency after just 3 hours of thermal treatment at 170 °C compared to colloidal forms that only converted 50% [16]. We verified that the structure of our thermal condensation product is also alanine anhydride, which makes the DTG peak ~ 165 °C a good indicator of the catalytic activity of each metal doped FSN sample. DTG curves are shown in Figure 6.

a)

b)
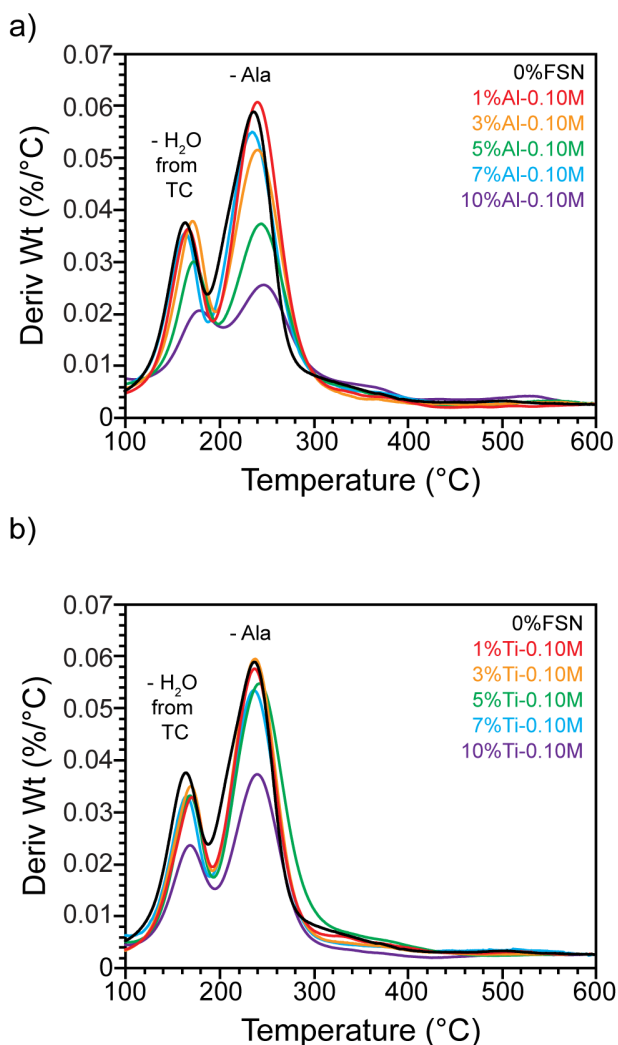
Figure 6. DTG curves of 0%FSN and (a) Al- and (b) Ti-doped FSN with 0.10M Ala adsorbed.

3% Al- and Ti-NPs had the largest TC peaks after 0%FSN. 10% dopants had greatly reduced intensity of TC and degradation peaks accompanied by line broadening which points to disorder at the surface causing thermal events to occur over a larger range of temperatures. To better compare the data, we define TC efficiency as molecules of water produced by thermal condensation over molecules ala adsorbed. The % weight loss was higher than 0%FSN for all dopants but once surface area was factored in, the number of adsorbed Ala molecules was less than 0%FSN for all dopants, and TC efficiency was also lower in dopants compared to 0%FSN. TC efficiency expresses small differences which help us determine how reactive each surface is

compared with 0%FSN and how much doping affects the chemistry at the surface. 10%Al performed the worst among the Al dopants. It had the lowest Ala adsorption and TC efficiency values, as well as the broadest peaks.

DTG peaks for Ti dopants showed less variation and the thermal events were well-defined and narrow, with 1% and 3%Ti performing comparably to 0%FSN. 10%Ti preforms the worst among Ti dopants with the lowest amount of adsorbed Ala molecules and the second smallest TC efficiency. It is interesting that in both ^{29}Si MAS NMR, Raman, and TGA the 5% dopants are outliers. 5%Ti in TGA data had the highest molecules adsorbed but lowest TC efficiency. 5%Ti also had the smallest Raman peaks.

Table 3. BET analysis and TGA calculations.

Doping Level	SSA (m^2 g^{-1})	Diameter (nm)	OH nm^{-2}	0.10M L-Ala		
				Wt Loss (%)	Molecules (/nm^2)	TC Efficiency
0%FSN	269	8.4	6.0	6.47	1.75	1.59
1%Al	334	6.7	2.8	7.00	1.53	1.41
3%Al	363	6.2	1.2	7.38	1.50	1.46
5%Al	363	6.0	1.0	6.86	1.39	1.42
7%Al	357	6.1	0.7	7.51	1.55	1.49
10%Al	357	6.0	1.8	6.60	1.35	1.30
1%Ti	339	6.6	4.5	6.40	1.37	1.36
3%Ti	346	6.4	5.0	6.77	1.43	1.40
5%Ti	338	6.5	2.6	7.58	1.66	1.25
7%Ti	348	6.3	1.7	7.08	1.50	1.40
10%Ti	361	5.9	1.0	6.17	1.24	1.36

4. Conclusion

The purpose of this study was to determine if Al- and Ti-doped FSN behave the same as commercial grade FSN. TGA was performed to analyze the adsorption potential and catalytic efficiency. All doped NPs had lower molecular adsorption (molecules nm^{-2}) and catalytic efficiency than 0%FSN. Negligible differences were observed in thermal condensation peak temperature, relative CP populations, and ^{29}Si Q_2 FWHM. ^{29}Si Q_3 and Q_4 FWHM measured by CP-MAS increased with doping level (300 – 400 Hz more broad than FSN). The ^{29}Si DP-MAS

chemical shift of Q_4 increased with doping level, which could be due to either larger Si-O-T bond angles, deshielding effects from Al/Ti, or both. Our data suggests that Al was incorporated into the framework in 1% and 3%Al and may congregate near the surface in 7% and 10%Al. Phase separation is possible in Ti dopings as ^{29}Si DP-MAS Q_4 intensities were all similar and clear anatase stretching modes were observed in Raman, indicating crystallinity. Paired with previous work, 1% and 3% Al- and Ti-doped FSN offer a less toxic alternative to commercial production with comparable performance.

5. Acknowledgements

6. Conflicts of Interest

The authors have no conflicts of interest to declare.

7. Supplementary Information

The online version contains supplementary material available at…

8. TOC Graphic

References

Uncategorized References

1. Regulations CoF (2020) 21. 1, vol B. Department of Health and Human Services, Code of Federal Regulations

2. Zhang H, Dunphy DR, Jiang X, Meng H, Sun B, Tarn D, Xue M, Wang X, Lin S, Ji Z, Li R, Garcia FL, Yang J, Kirk ML, Xia T, Zink JI, Nel A, Brinker CJ (2012) Processing pathway dependence of amorphous silica nanoparticle toxicity: colloidal vs pyrolytic. J Am Chem Soc 134 (38):15790-15804. doi:10.1021/ja304907c

3. Sun B, Pokhrel S, Dunphy DR, Zhang H, Ji Z, Wang X, Wang M, Liao YP, Chang CH, Dong J, Li R, Madler L, Brinker CJ, Nel AE, Xia T (2015) Reduction of Acute Inflammatory Effects of Fumed Silica Nanoparticles in the Lung by Adjusting Silanol Display through Calcination and Metal Doping. ACS Nano 9 (9):9357-9372. doi:10.1021/acsnano.5b03443

4. Sun B, Wang X, Liao YP, Ji Z, Chang CH, Pokhrel S, Ku J, Liu X, Wang M, Dunphy DR, Li R, Meng H, Madler L, Brinker CJ, Nel AE, Xia T (2016) Repetitive Dosing of Fumed Silica Leads to Profibrogenic Effects through Unique Structure-Activity Relationships and Biopersistence in the Lung. ACS Nano 10 (8):8054-8066. doi:10.1021/acsnano.6b04143

5. Tallant DR, Bunker BC, Brinker CJ, Balfe CA (1986) Raman Spectra of Rings in Silicate Materials. MRS Proceedings 73:261. doi:10.1557/PROC-73-261

6. McKee AD, Solano M, Saydjari A, Bennett CJ, Hud NV, Orlando TM (2018) A Possible Path to Prebiotic Peptides Involving Silica and Hydroxy Acid-Mediated Amide Bond Formation. Chembiochem 19 (18):1913-1917. doi:10.1002/cbic.201800217

7. Brack A (2007) From interstellar amino acids to prebiotic catalytic peptides: a review. Chem Biodivers 4 (4):665-679. doi:10.1002/cbdv.200790057

8. Rode BM (1999) Peptides and the origin of life. Peptides 20 (6):773-786

9. Bujdak J, Eder A, Yongyai Y, Faybikova K, Rode BM (1996) Investigation on the mechanism of peptide chain prolongation on montmorillonite. J Inorg Biochem 61 (1):69-78

10. Erastova V, Degiacomi MT, D GF, Greenwell HC (2017) Mineral surface chemistry control for origin of prebiotic peptides. Nat Commun 8 (1):2033. doi:10.1038/s41467-017-02248-y

11. Lambert JF (2008) Adsorption and polymerization of amino acids on mineral surfaces: a review. Orig Life Evol Biosph 38 (3):211-242. doi:10.1007/s11084-008-9128-3

12. Rimola A, Costa D, Sodupe M, Lambert JF, Ugliengo P (2013) Silica surface features and their role in the adsorption of biomolecules: computational modeling and experiments. Chem Rev 113 (6):4216-4313. doi:10.1021/cr3003054

13. Meng M, Stievano L, Lambert J-F (2004) Adsorption and Thermal Condensation Mechanisms of Amino Acids on Oxide Supports. 1. Glycine on Silica. Langmuir 20 (22):914-923. doi:10.1021/la035336b

14. Lahav N, White D, Chang S (1978) Peptide formation in the prebiotic era: thermal condensation of glycine in fluctuating clay environments. Science 201 (4350):67-69. doi:10.1126/science.663639

15. Liebau F (2012) Structural chemistry of silicates: structure, bonding, and classification. Springer Science & Business Media,

16. Guo C, Jordan JS, Yarger JL, Holland GP (2017) Highly Efficient Fumed Silica Nanoparticles for Peptide Bond Formation: Converting Alanine to Alanine Anhydride. ACS Appl Mater Interfaces 9 (20):17653-17661. doi:10.1021/acsami.7b04887

17. Swanson HL, Guo C, Cao M, Addison JB, Holland GP (2020) Probing the binding modes and dynamics of histidine on fumed silica surfaces by solid-state NMR. Phys Chem Chem Phys 22 (36):20349-20361. doi:10.1039/d0cp03472j

18. Bouchoucha M, Jaber M, Onfroy T, Lambert J-F, Xue B (2011) Glutamic Acid Adsorption and Transformations on Silica. The Journal of Physical Chemistry C 115 (44):21813-21825. doi:10.1021/jp206967b

19. Lambert JF, Jaber M, Georgelin T, Stievano L (2013) A comparative study of the catalysis of peptide bond formation by oxide surfaces. Phys Chem Chem Phys 15 (32):13371-13380. doi:10.1039/c3cp51282g

20. Liu CHC, Maciel GE (1996) The fumed silica surface: A study by NMR. Journal of the American Chemical Society 118 (21):5103-5119. doi:DOI 10.1021/ja954120w

21. Burkett SL, Sims SD, Mann S (1996) Synthesis of hybrid inorganic-organic mesoporous silica by co-condensation of siloxane and organosiloxane precursors. Chemical Communications (11):1367-1368. doi:DOI 10.1039/cc9960001367

22. van der Graaff WNP, Olvera KG, Pidko EA, Hensen EJM (2014) Stability and catalytic properties of porous acidic (organo)silica materials for conversion of carbohydrates. Journal of Molecular Catalysis A: Chemical 388-389:81-89. doi:10.1016/j.molcata.2013.11.013

23. Merzbacher CI, Sherriff BL, Hartman JS, White WB (1990) A high-resolution 29Si and 27Al NMR study of alkaline earth aluminosilicate glasses. Journal of Non-Crystalline Solids 124:194-206

24. Legrand AP, Taibi H, Hommel H, Tougne P, Leonardelli S (1993) Silicon functionality distribution on the surface of amorphous silicas by 29Si solid state NMR. Journal of Non-Crystalline Solids 155:122-130

25. Ramdas S, Klinowski J (1984) A simple correlation between isotropic 29Si-NMR chemical shifts and T-O-T angles in zeolite frameworks. Nature 308:521-523

26. Oestrike R, Yang W, Kirkpatrick RJ, Hervig RL, Navrotsky A, Montez B (1987) High-resolution 23Na, 27Al, 29Si NMR spectroscopy of framework aluminosilicate glasses. Geochimica et Cosmochimica Acta 51:2199-2209

27. Balmer ML, Bunker BC, Wang LQ, Peden CHF, Su Y (1997) Solid-State 29Si MAS NMR Study of Titanosilicates. Journal of Physical Chemistry B 101:9170-9179

28. Hanaor DAH, Sorrell CC (2010) Review of the anatase to rutile phase transformation. Journal of Materials Science 46 (4):855-874. doi:10.1007/s10853-010-5113-0

29. Sandstrom DR, Lytle FW, Wei PSP, Greegor RB, Wong J, Schultz P (1980) Coordination of Ti in TiO2-SiO2 Glass by X-Ray Absorption Spectroscopy. Journal of Non-Crystalline Solids 41:201-207

30. Greegor RB, Lytle FW, Sandstrom DR, Wong J, Schultz P (1983) Investigation of TiO2-SiO2 Glasses by X-Ray Absorption Spectroscopy. Journal of Non-Crystalline Solids 55:27-43

31. Schneider E, Wong J, Thomas JM (1991) Multinuclear solid state NMR investigation of titanium-containing silicate glasses. Journal of Non-Crystalline Solids 136:1-13

32. Dupree R, Pettifer RF (1984) Determination of the Si-O-Si Bond Angle Distribution in Vitreous Silica by Magic Angle Spinning Nmr. Nature 308 (5959):523-525. doi:DOI 10.1038/308523a0

33. Brinker CJ, Kirkpatrick RJ, Tallant DR, Bunker BC, Montez B (1988) NMR Confirmation of Strained "Defects" in Amorphous Silica. Journal of Non-Crystalline Solids 99:418-428

34. Smith JV, Blackwell CS (1983) Nuclear Magnetic-Resonance of Silica Polymorphs. Nature 303 (5914):223-225. doi:DOI 10.1038/303223a0

35. Autschbach J, Zheng S, Schurko RW (2010) Analysis of electric field gradient tensors at quadrupolar nuclei in common structural motifs. Concepts in Magnetic Resonance Part A 36A (2):84-126. doi:10.1002/cmr.a.20155

36. Ashbrook SE, Duer MJ (2006) Structural information from quadrupolar nuclei in solid state NMR. Concepts in Magnetic Resonance Part A 28A (3):183-248. doi:10.1002/cmr.a.20053

37. Ray GJ, Samoson A (1993) Double rotation and variable field 27Al NMR study of dealuminated Y zeolites. Zeolites 13:410-413

38. Deng F, Du Y, Ye C, Wang J, Ding T, Li H (1995) Acid Sites and Hydration Behavior of Dealuminated Zeolite HZSM-5: A High-Resolution Solid State NMR Study. Journal of Physical Chemistry 99:15208-15214

39. Huang J, van Vegten N, Jiang Y, Hunger M, Baiker A (2010) Increasing the Bronsted acidity of flame-derived silica/alumina up to zeolitic strength. Angew Chem Int Ed Engl 49 (42):7776-7781. doi:10.1002/anie.201003391

40. Kanellopoulos J, Unger A, Schwieger W, Freude D (2006) Catalytic and multinuclear MAS NMR studies of a thermally treated zeolite ZSM-5. Journal of Catalysis 237 (2):416-425. doi:10.1016/j.jcat.2005.11.030

41. Massiot D, Bessada C, Coutures JP, Taulelle F (1990) Quantitative study of 27Al MAS NMR in crystalline YAG. Journal of Magnetic Resonance 90:231-242

42. Lookman R, Grobet P, Merckx R, Van Riemsdijk WH (1997) Application of 31P and 27Al MAS NMR for phosphate speciation studies n soil and aluminum hydroxides: promises and constraints. Geoderma 80:369-388

43. Singh PS, Bastow T, Trigg M (2005) Structural studies of geopolymers by 29Si and 27Al MAS-NMR. Journal of Materials Science 40:3951-3961

44. Geissberger AE, Galeener FL (1983) Raman studies of vitreous SiO2 versus fictive temperature. Physical Review B 28 (6):3266-3271. doi:10.1103/PhysRevB.28.3266

45. Vaccaro G, Angnello S, Buscarino G, Gelardi FM (2010) Thermally Induced Structural Modifications of Silica Nanoparticles Investigated by Raman and Infrared Absorption Spectroscopies. J Phys Chem C 114:13991-13997

46. Huang PJ, Chang H, Yeh CT, Tsai CW (1997) Phase transformation of TiO2 monitored by Thermo-Raman spectroscopy with TGA/DTA. Thermochimica Acta 297:85-92

47. Meng M, Stievano L, Lambert JF (2004) Adsorption and Thermal Condensation Mechanisms of Amino Acids on Oxide Supports. 1. Glycine on Silica. Langmuir 20:914-923

48. Bujdak J (1996) The effect of reaction conditions on montmorillonite-catalysed peptide formation. Catalysis Letters 37:267-272

49. Fuchida S, Masuda H, Shinoda K (2014) Peptide formation mechanism on montmorillonite under thermal conditions. Orig Life Evol Biosph 44 (1):13-28. doi:10.1007/s11084-014-9359-4

50. Guo C, Holland GP (2015) Alanine Adsorption and Thermal Condensation at the Interface of Fumed Silica Nanoparticles: A Solid-State NMR Investigation. The Journal of Physical Chemistry C 119 (45):25663-25672. doi:10.1021/acs.jpcc.5b10236

51. Lambert J-F, Stievano L, Lopes I, Gharsallah M, Piao L (2009) The fate of amino acids adsorbed on mineral matter. Planetary and Space Science 57 (4):460-467. doi:https://doi.org/10.1016/j.pss.2009.01.012

52. Stievano L, Piao LY, Lopes I, Meng M, Costa D, Lambert JF (2007) Glycine and lysine adsorption and reactivity on the surface of amorphous silica. European Journal of Mineralogy 19 (3):321-331. doi:10.1127/0935-1221/2007/0019-1731

53. Guo C, Holland GP (2014) Investigating Lysine Adsorption on Fumed Silica Nanoparticles. The Journal of Physical Chemistry C 118 (44):25792-25801. doi:10.1021/jp508627h

54. Rimola A, Tosoni S, Sodupe M, Ugliengo P (2006) Does silica surface catalyse peptide bond formation? New insights from first-principles calculations. Chemphyschem 7 (1):157-163. doi:10.1002/cphc.200500401